

# Covarying Hydroclimate Patterns between Monsoonal Asia and North America over the Past 600 Years

KEYAN FANG

*Department of Geosciences and Geography, University of Helsinki, Helsinki, Finland, and Key Laboratory of Humid Subtropical Eco-geographical Process (Ministry of Education), College of Geographical Sciences, Fujian Normal University, Fuzhou, China*

DELIANG CHEN

*Department of Earth Sciences, University of Gothenburg, Gothenburg, Sweden*

JINBAO LI

*Department of Geography, University of Hong Kong, Hong Kong, China*

HEIKKI SEPPÄ

*Department of Geosciences and Geography, University of Helsinki, Helsinki, Finland*

(Manuscript received 14 May 2013, in final form 22 November 2013)

## ABSTRACT

Proxy data with large spatial coverage spanning to the preindustrial era not only provide invaluable material to investigate hydroclimate changes in different regions but also enable studies on temporal changes in the teleconnections between these regions. Applying the singular value decomposition (SVD) method to tree-ring-based field reconstructions of the Palmer drought severity index (PDSI) over monsoonal Asia (MA) and North America (NA) from 1404 to 2005, the dominant covarying pattern between the two regions is identified. This pattern is represented by the teleconnection between the dipole pattern of southern–northern latitudinal MA and the dipole of southwest NA (SWNA)–northwest NA (NNA), which accounts for 59.6% of the total covariance. It is dominated by an antiphase low MA and SWNA teleconnection, driven by the El Niño–Southern Oscillation (ENSO), and is most significant at an interannual time scale. This teleconnection is strengthened (weakened) in periods of increased (decreased) solar forcing and high (low) temperature, which is associated with intensified (weakened) ENSO variability. Additional forcing by SST anomalies in the Indian and western Pacific Oceans appears to be important too.

## 1. Introduction

Teleconnections in climatology are an example of the nonlinearity of the Earth System that connects climate anomalies over a long distance (thousands of kilometers) (Trenberth et al. 1998). Teleconnections have received much attention in recent decades because understanding their roles can help improve the climate predictability (Ding and Wang 2005; Lau and Weng 2002; Trenberth et al. 1998). During the instrumental

period, hydroclimate changes between monsoonal Asia (MA) and North America (NA) are linked by the Walker circulation in the low latitudes (Fang et al. 2011b; Feng and Hu 2004; Kumar et al. 1999; Ummenhofer et al. 2012) and by the zonally elongated height anomalies from northeastern Asia to NA in the middle troposphere and the wave train possibly stemming from Rossby wave dispersion from the Indo-Pacific region in the midlatitudes (Lau and Weng 2002). These atmospheric teleconnections are regulated by sea surface temperature (SST) patterns such as those associated with El Niño (Herweijer and Seager 2008; Hoerling and Kumar 2003; Lau and Weng 2002; Seager 2007). However, the temporal stability of these covarying patterns as well as the key ocean–atmosphere

---

*Corresponding author address:* Keyan Fang, Department of Geosciences and Geography, P.O. Box 64, 00014 University of Helsinki, Helsinki, Finland.  
E-mail: kujanfan@gmail.com

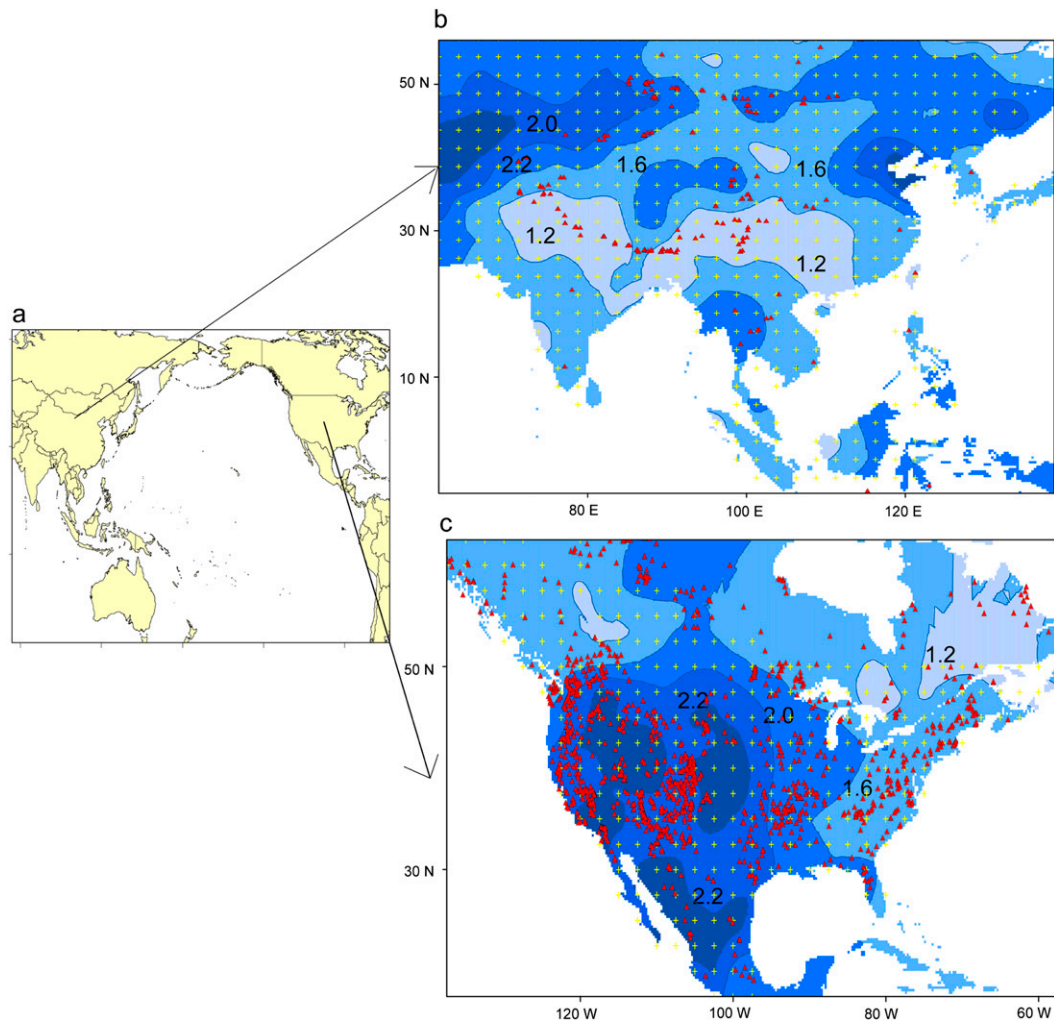


FIG. 1. (a) The locations of the study regions in pan-Pacific areas and the standard deviation of the reconstructed PDSI of the (b) MADA and (c) NADA over the overlapping period 1404–2005 for most of the grids in both datasets. The grid points in MADA and NADA are indicated by crosses and the tree-ring records are indicated by triangles. The standard deviations are indicated by the shaded areas and their values are shown near the contours.

patterns associated with these teleconnections remain unclear due to the limited instrumental records.

Tree-ring-based climate-field reconstructions are invaluable to extend the instrumental records centuries or millennia back in time over large areas (Cook et al. 1999, 2007, 2010; Fang et al. 2011a), owing to their annual resolution and evenly gridded spatial distribution that facilitates climatic diagnostic analyses and comparisons with the model outputs (Fang et al. 2012; Ummenhofer et al. 2012). As for the MA and NA, the availability of the tree-ring-based North American Drought Atlas (NADA) (Cook et al. 1999, 2004) and the Monsoon Asia Drought Atlas (MADA) (Cook et al. 2010) enable investigations on regional hydroclimate changes (Cook et al. 2007; Fang et al. 2012; Li et al. 2014, 2011). Yet, investigations focusing on the covariability between MA

and NA remain to be done. Here we use the MADA and NADA to explore their hydroclimate teleconnections in relation to the ocean surface thermal condition and atmospheric circulation. Our aims are to 1) investigate the time-varying hydroclimate covariability between MA and NA over the past six centuries and 2) explore potential mechanisms associated with these teleconnections by examining the associations between the hydroclimatic covariability and the SST, geopotential heights (GPHs), and winds in the middle troposphere.

## 2. Data and methods

### a. Tree-ring-based drought reconstructions

The target drought variable used in the MADA and NADA is a meteorological drought index, the Palmer

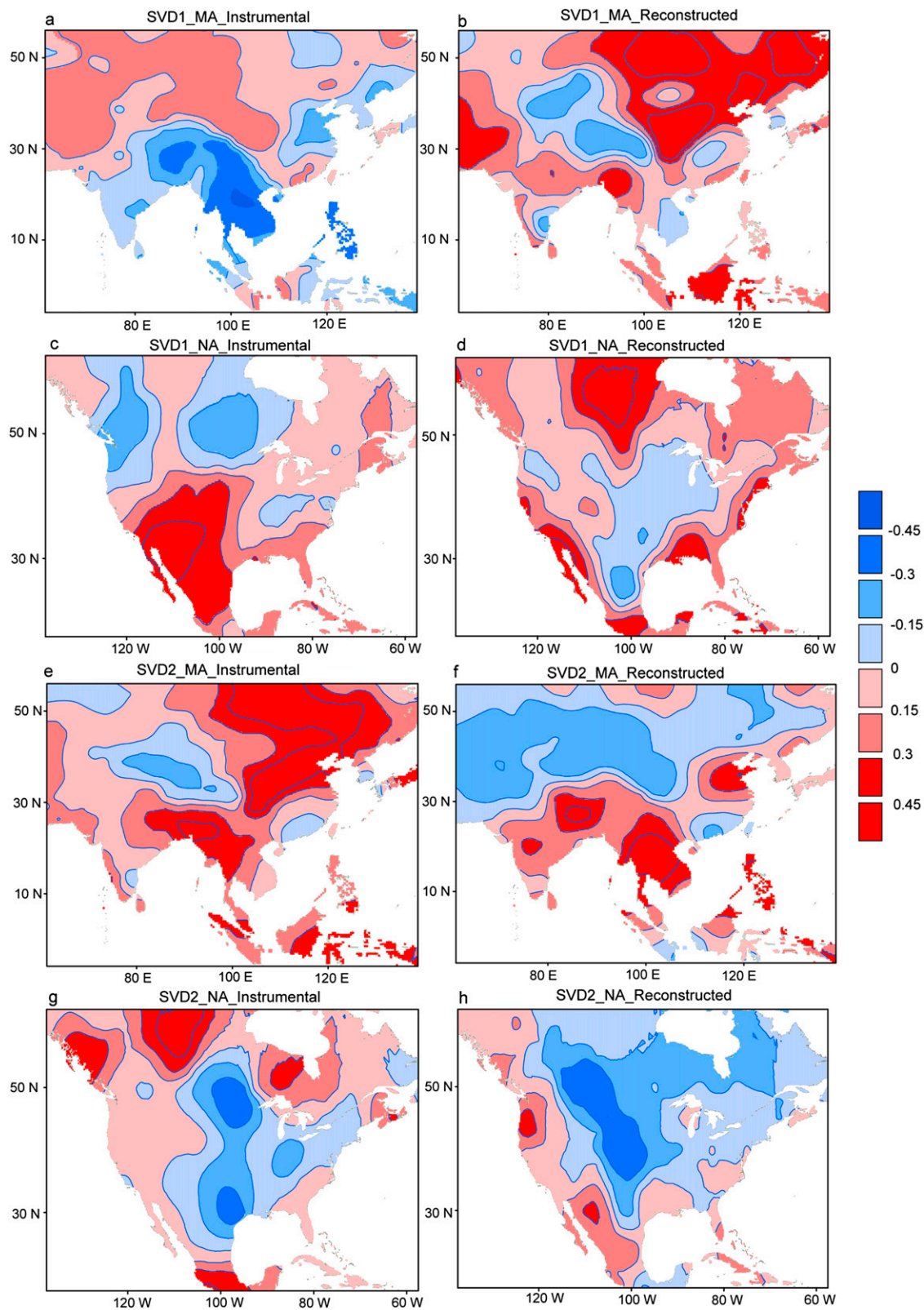


FIG. 2. Comparisons of the heterogeneous correlation maps for the first two leading SVD modes between monsoonal Asia and North America for both (left) instrumental and (right) reconstructed (MADA and NADA datasets) PDSI over the common period 1951–2005. The significance levels of 0.05 and 0.01 for the correlations are about 0.27 and 0.35, respectively.

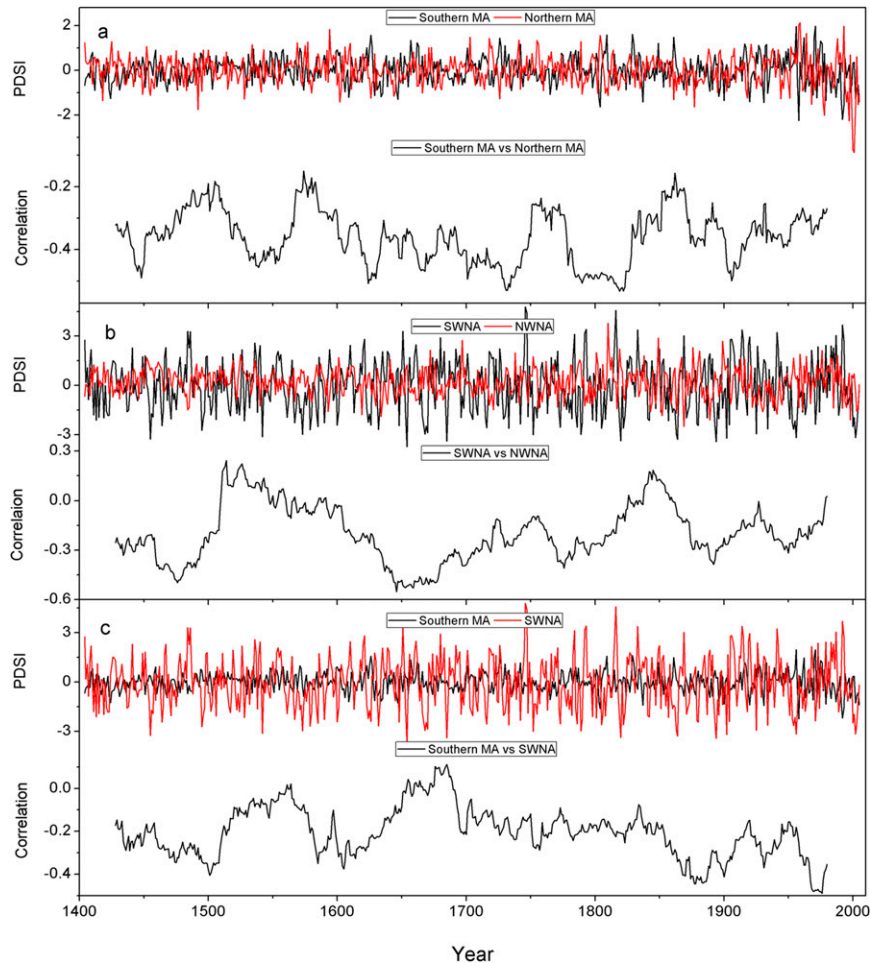


FIG. 3. Visual comparisons and the running correlations based on a 50-yr window (a) between the regional PDSI averaged from southern ( $10^{\circ}$ – $30^{\circ}$ N) and northern ( $30^{\circ}$ – $50^{\circ}$ N) MA, (b) between NWNA (north of  $45^{\circ}$ N and east of  $110^{\circ}$ W) and SWNA (south of  $40^{\circ}$ N and east of  $95^{\circ}$ W), and (c) between southern MA and SWNA.

drought severity index (PDSI), derived from a global dataset with  $2.5^{\circ} \times 2.5^{\circ}$  resolution (Dai et al. 2004), which was scaled to allow direct spatiotemporal comparisons of moisture conditions of diverse climates (Wells et al. 2004). The PDSI shows degraded skill in representing moisture conditions in cold regions or in winter with snowfall and droughts of a short duration (Dai et al. 2004; Wells et al. 2004). Thereby, the summer (June–August) PDSI was reconstructed in both the MADA and NADA (Cook et al. 1999, 2007, 2004, 2010). In MADA, 327 tree-ring chronologies were used to reconstruct 534 PDSI grids (Cook et al. 2010), while in NADA 1845 chronologies were employed to reconstruct 286 grid points in its most recent version (NADA v2a) (Cook et al. 2004).

Both reconstructions were based on a point-by-point regression (PPR) method to locate the nearby chronologies

to reconstruct PDSI in each grid. Accordingly, the reconstruction is generally more robust for a grid with more tree-ring chronologies in neighboring regions, and the reliability of a reconstruction with limited tree-ring records is largely dependent on the robustness of the teleconnection between target PDSI grid and remote tree-ring chronologies. In MADA, most of the chronologies are in the southern and eastern boundaries of the Tibetan Plateau, central and western Mongolia, and the Altai Mountains (Fig. 1b), but the general hydroclimate patterns in various climates in MA can be well reconstructed (Fang et al. 2012). Tree-ring chronologies in NADA are relatively evenly distributed (Fig. 1c). The MADA and NADA generally show a normal distribution with small portions of extreme wetness ( $>6$ ) or dryness ( $<-6$ ) (Cook et al. 2007; Fang et al. 2012; Li et al. 2014). To facilitate the implementation of the SVD



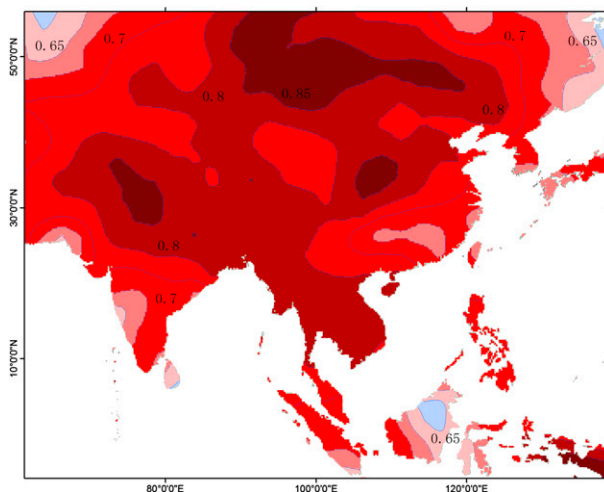


FIG. 4. Correlations between the instrumental and reconstructed PDSI data during the common period 1951–2005.

analyses (details shown below) that require even time span of all grids, we employed the overlapping period from 1404 to 2005 covering 510 PDSI grids of the MADA and 266 grids of the NADA data, which include as many PDSI grids as possible and as long time duration as possible.

#### *b. Data for ocean surface temperature and atmospheric circulations*

We employed the extended reconstructed SST, version 3b (ERSST.v3b) (Smith et al. 2008) data with a  $2^\circ \times 2^\circ$  resolution starting from 1854 to identify the relationship between ocean thermal conditions and the hydroclimate teleconnections. One caution is that the quality of this dataset is dampened before 1870 owing to the limited availability of data (Smith et al. 2008). We further detect the relationships between hydroclimate changes and atmospheric circulations using the GPH and wind vectors at 500 hPa of the Twentieth Century Reanalysis (version 2) data since January 1871 (Compo et al. 2011). These data are provided by the National Centers for Environmental Prediction–National Center for Atmospheric Research (NCEP–NCAR) (Kalnay et al. 1996; Kistler et al. 2001). It was selected because it has been widely tested (Duan and Wu 2005; Sturaro 2003) and because of its long time duration that enables investigations of temporal evolution of the teleconnections.

#### *c. Singular value decomposition*

Singular value decomposition (SVD) is widely used in climatology to investigate coupled modes between two climatic fields with interpretable results (Bretherton et al. 1992), fitting our need to detect the covariability between hydroclimate changes in MA and NA. The

cross-covariance matrix is generated between the two fields for consideration, which is decomposed into the rotation matrices of the left-singular vectors and the right-singular vectors and the scaling matrix of the rectangular diagonal matrix. The nonzero singular values from the diagonal entries of the rectangular matrix determine the importance of the decomposed coupled modes. One can extract the key coupled modes between two climate fields by only retaining the coupled modes with large squared covariance, which is determined by the ratios between the squared singular values and their sum (Bretherton et al. 1992). The correlations between the two transformed fields by SVD decomposition are calculated to indicate their relationships for SVD modes. The heterogeneous correlation maps are calculated between a time series of a transformed field and the other climate field to indicate key regions accounting for the covariability, which can be used to identify the key regions accounting for connection between the two fields. The SVD is implemented with the MADA as the left field and the NADA as the right field. The climatic meanings of the SVD modes were analyzed bearing in mind that there can be SVD modes with only statistical meanings (Yang and Lau 2004).

### **3. Covariability during the instrumental and reconstructed periods**

#### *a. Testing the reconstructions in reproducing the covarying patterns*

We first compare the SVD modes of the instrumental and reconstructed PDSI since 1951, a period with reliable instrumental records for both the MA and NA (Cook et al. 2010; Fang et al. 2010; Li et al. 2009), to test the ability of the reconstructions in reproducing the instrumental SVD patterns (Fig. 2). The first two leading SVD modes of the instrumental PDSI explain 52.3% and 14.2% of the MADA–NADA covariance. Heterogeneous correlation maps of the first SVD mode indicate the positive correlations in northern MA and negative correlations in the southern Asia, particularly for the Indochina region (Fig. 2a). This large-scale pattern is termed the southern–northern MA dipole. This dipole pattern is also seen via comparisons of the regionally averaged PDSI between the southern and northern MA (Fig. 3). Accordingly, significant positive correlations are observed in the southwest NA (SWNA) and negative correlations in the northwestern NA (NWNNA), which is referred as the SWNA–NWNNA dipole (Fig. 2c). This dipole pattern is less significant as indicated by the relatively weak heterogeneous correlations over NWNNA and the less significant negative correlations between the averaged PDSI of NWNNA and SWNA

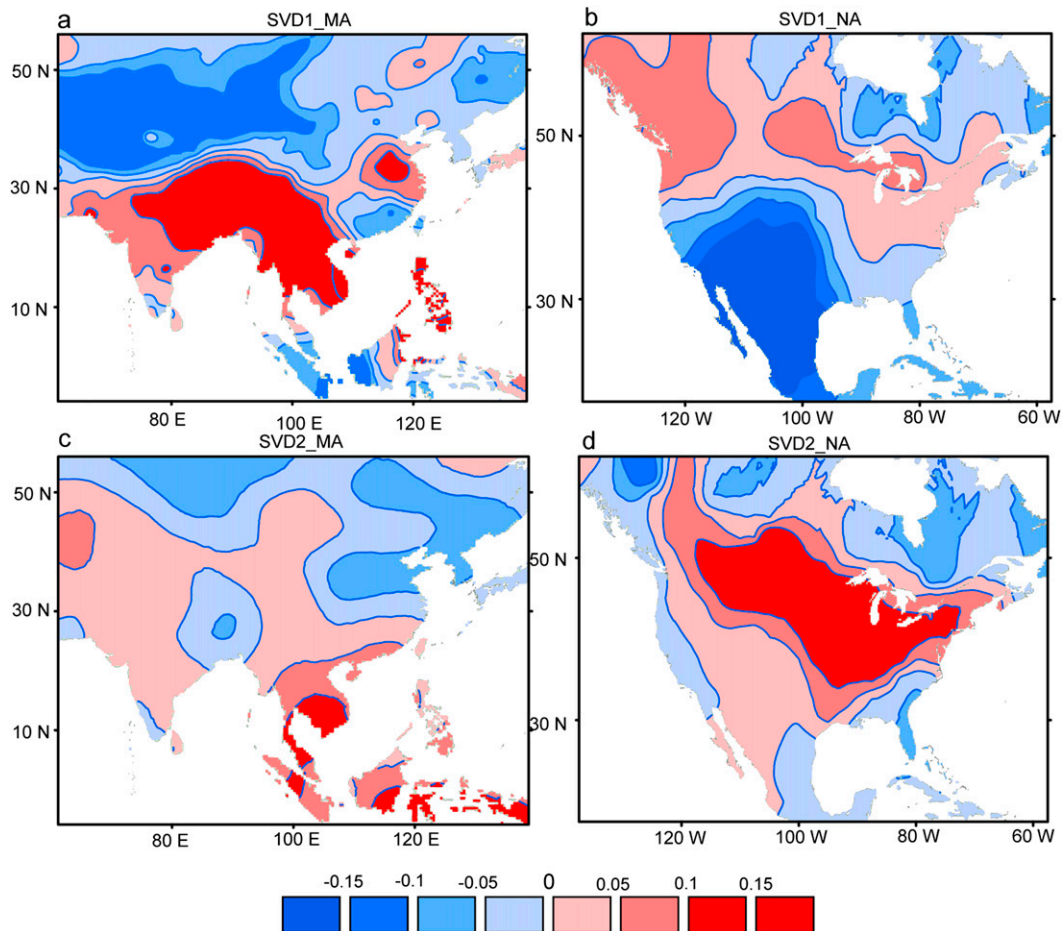


FIG. 5. Heterogeneous correlation maps for the first two leading SVD modes between (a),(c) MADA and (b),(d) NADA during their common periods covering most grid cells from 1404 to 2005. The correlations at 0.05 and 0.01 significant levels are around 0.08 and 0.11, respectively.

(Fig. 3). The two dipole patterns in MA and NA are closely linked, which is termed the southern–northern MA and SWNA–NNA teleconnection. In this teleconnection, the southern MA and the SWNA are reversely correlated as indicated by the heterogeneous correlation maps (Fig. 2) and the correlations of the averaged PDSI between the two regions (Fig. 3). The second SVD mode of the instrumental data shows a horseshoelike positive correlation pattern in northern MA (northeastern Asia). Accordingly, significantly positive correlations are observed in northern NA (Figs. 2b,d). The northern MA (northeastern Asia) pattern and northern NA pattern are positively correlated.

There may be uncertainties in the teleconnection inferred from reconstructions owing to the scarcity of tree-ring data for some regions, particularly for MADA, although the reconstructed and the instrumental data show significant correlation over most of the regions (Fig. 4). First, most of the tree-ring chronologies

are from the middle and high latitudes; therefore, the reconstructions can better recover the hydroclimate variability of the high latitudes. Accordingly, teleconnections calculated from the reconstructed data are more conspicuous over the high latitudes than those calculated from the instrumental data over their common period (Fig. 2). However, during the entire reconstructed period the teleconnection is centered in the low latitudes. This suggests that this bias can be neglected when studying the teleconnection over the entire reconstruction period. Second, previous investigations have mentioned that the MADA has limited ability in recovering the hydroclimate variability for southeastern China, central Inner Mongolia, and south-central Mongolia (Fang et al. 2012). The weak signal strength from southeastern China may bias the teleconnection pattern between southern China and NA. Anyway, high correlations are also observed near southeastern China. Hydroclimate in central Inner Mongolia and south-central Mongolia has

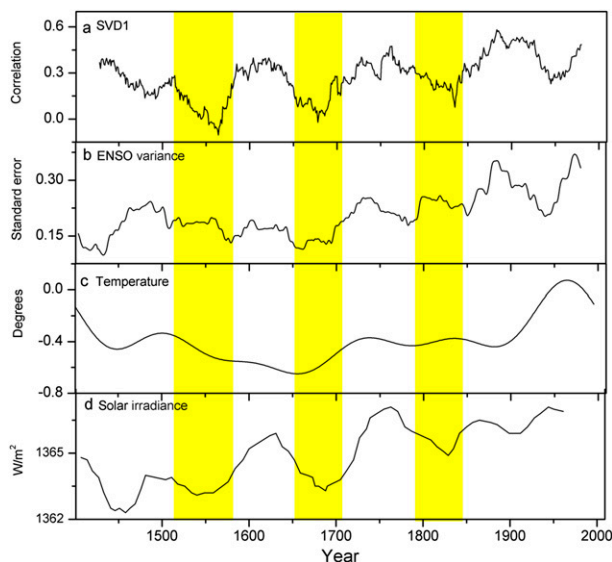


FIG. 6. Moving correlations based on a 50-yr window between (a) the paired SVD time series of the first SVD modes of the MADA and NADA, (b) the time series of variances of ENSO reconstruction for the Niño-3.4 region (Mann et al. 2009), (c) the low-passed ( $<0.01$  Hz) annual mean temperature reconstruction (Mann et al. 2009), and (d) the reconstruction of solar irradiance (Bard et al. 2000).

limited contributions to the teleconnection. Therefore, the weak signals strength from the two regions should have limited influences on the large-scale teleconnections. Taken together, we consider that the MADA and NADA can generally reproduce the patterns of the hydroclimate teleconnections since the biases in reconstructions are at regional scale and have limited influences on the large-scale teleconnection pattern.

The southern–northern MA dipole is similar to the southern Asia–central Asia dipole, the leading principal component of the MADA, which has been identified in a previous study (Li et al. 2014). The monsoon dynamics do not result in even hydroclimate changes in the southern MA. Within this dipole, there is a reverse pattern between southeastern and northern China owing to the shift of the western Pacific subtropical high with its northerly (southerly) displacement being accompanied by dry (pluvial) southeastern China and pluvial (dry) northern China (Fang et al. 2011b; Lu 2005; Yang and Lau 2004). The SWNA–NWN dipole is also observed for NA as the second principal component pattern for NADA (Li et al. 2014). Both support the heterogeneous maps of the leading SVD modes. One difference between the teleconnection and the dominant drought patterns is that more significant loadings of the principal components of MA and NA are observed in the high-latitude regions, while the southern–northern MA and

SWNA–NWN dipole has higher loadings in the low-latitude regions. This probably indicates that this teleconnection pattern is linked via the low latitudes. One should be noted that the teleconnection may contain some signal from winter because the summer PDSI can incorporate the influences of winter precipitation, particularly for SWNA (St. George et al. 2010).

A previous study has identified key teleconnection regions in the Yangtze River region in MA and the northern Great Plains and Midwest in NA with in-phase precipitation variations (Lau and Weng 2002), which is different from this study. The major reason is that Lau and Weng (2002) excluded the tropical areas: for example, the Indian subcontinent, the Indochina region, and the Mexican area. Another factor may be associated with the uneven distribution of the tree-ring records in MADA with only one tree-ring chronology in the Yangtze River region (Fig. 1b), which weakens the ability to reconstruct the climate variability in this region. Previous investigations also indicated that the hydroclimate patterns in Yangtze River regions were not well recovered (Fang et al. 2012). The heterogeneous correlation patterns of the first (second) SVD mode for the reconstructions are similar to the second (first) SVD modes of the instrumental data. The reconstructed datasets can generally recover the major covarying hydroclimate patterns shown in the instrumental data, except for the lack of the SWNA–NWN dipole (Fig. 2). The high loadings over northeastern Asia account for a larger variance in the reconstructions (first SVD mode) than in the instrumental data (second SVD mode). This is caused by the fact that the tropical signal strength in the MADA is weaker than the instrumental data due to the scarcity of tree-ring records in these hot and humid regions (Cook et al. 2010; Fang et al. 2012). Therefore, the teleconnection pattern in the reconstruction appears stronger in the middle and high latitudes with reduced signal strength in the tropical and the Yangtze River region. This may also be related to stronger variability in the middle and high latitudes, such as central Asia, northeastern Asia, and southeastern Asia in MADA and northwestern NA in NADA, as indicated by the spatial distributions of standard deviations (Fig. 1). However, it should be noted that the magnitudes of the standard deviations of MADA may be reduced by the ensemble PPR method when averaging together a number of reconstructions.

#### *b. Temporal covariability between MADA and NADA*

We further examined the covariability between MADA and NADA over the reconstruction period 1404–2005. The first leading SVD mode is the southern–northern MA



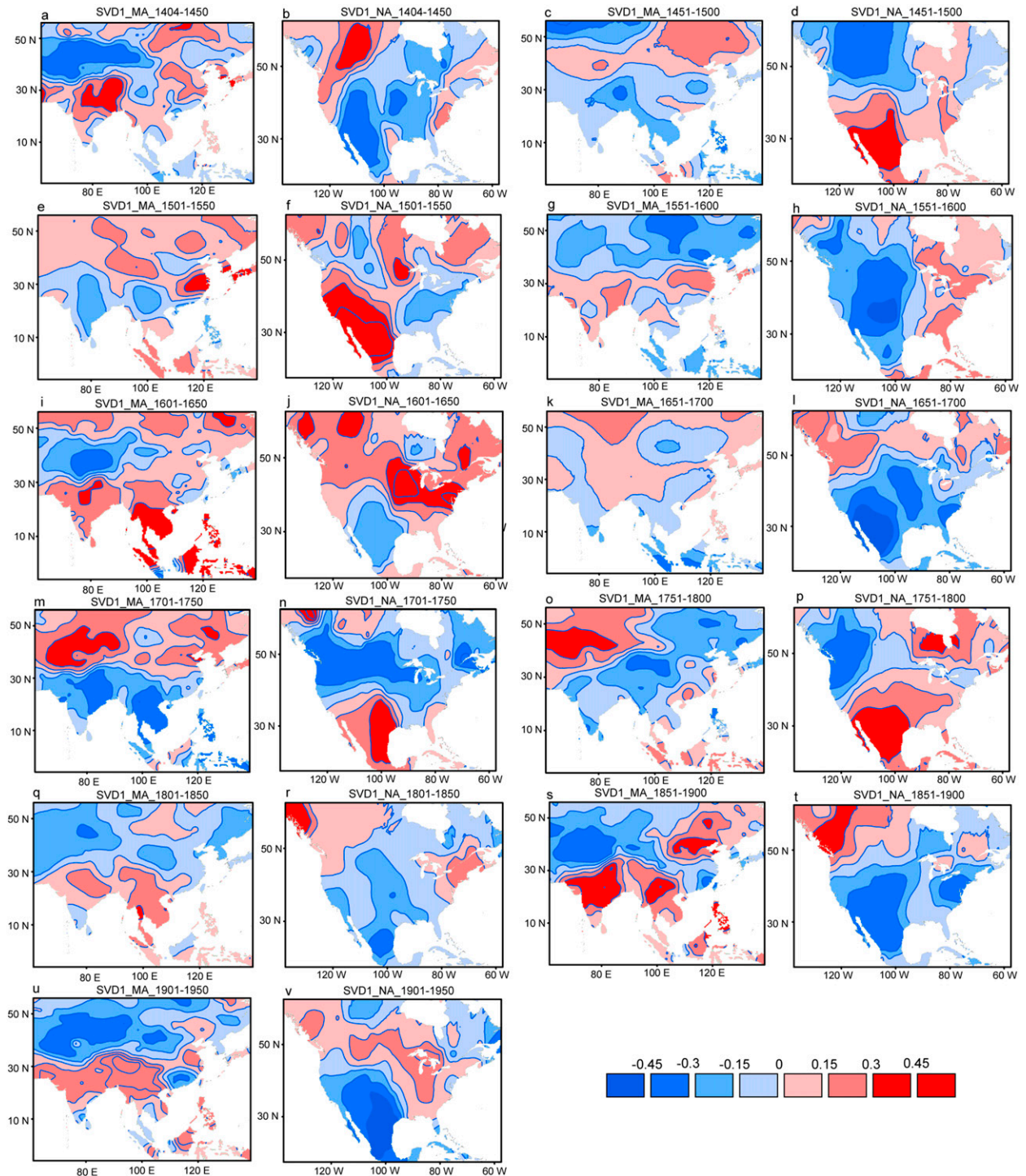


FIG. 7. Heterogeneous correlation maps for the MA and NA derived from the first leading SVD mode between MADA and NADA based on an around a 50-yr time interval. The most recent SVD mode for the period 1951–2005 is shown in Fig. 2.

and SWNA–NNA teleconnection, which explains 59.6% of the total covariance (Figs. 5a,b). This suggests that this teleconnection pattern is most robust over the range of time scales even though the reconstructions

tend to show higher teleconnection strength in the middle and high latitudes as indicated above. The higher loadings in the low latitudes again support the important role of linkages in low latitudes in establishing this



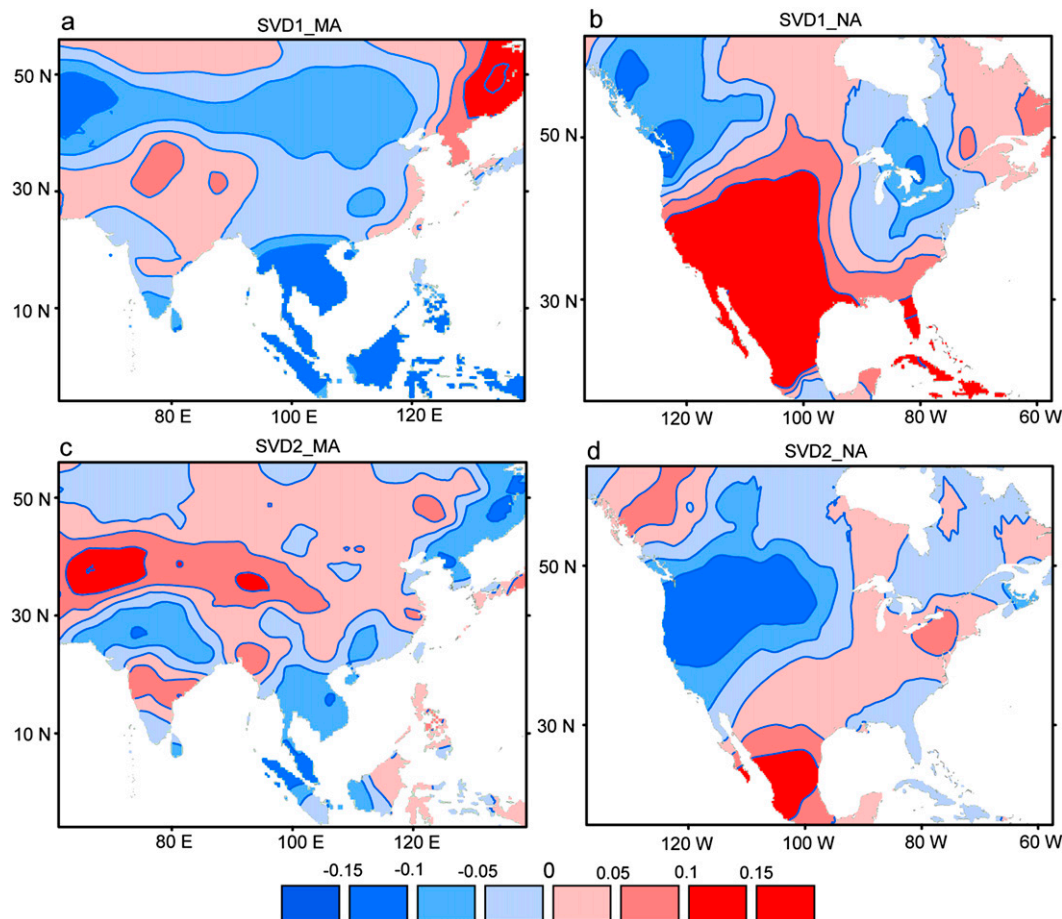


FIG. 8. Heterogeneous correlation maps for the first two leading SVD modes between (a),(c) MADA and (b),(d) NADA for the high-passed data ( $<8$  yr). The correlations at 0.05 and 0.01 significant levels are around 0.08 and 0.11, respectively.

teleconnection. The second SVD mode shows relatively high loadings over Indochina and central NA (Figs. 5c, d). Running correlations between time series of the first leading SVD mode were calculated to examine its temporal evolution and key forcings. The strength of the teleconnection generally increases toward the present (Fig. 6a), consistently with the generally increasing trend of solar irradiance and temperature from the Little Ice Age (1350–1850) to modern periods (Bard et al. 2000; Mann et al. 2009; Shindell et al. 2001). The lowest correlations for the first SVD modes are found near 1550, the latter half of the seventeenth century, and the early half of the nineteenth century (Fig. 6). These periods with weakened teleconnection correspond to the Spörer Minimum (1420–1570), the Maunder Minimum (1645–1715) and the end of the Little Ice Age in the 1850s (Bard et al. 2000; Eddy 1976; Shindell et al. 2001). These periods with weakened solar activity are often associated with low temperature (Mann et al. 2009). The

strength of the southern–northern MA and SWNA–NWNA teleconnection varies through time and appears to strengthen (weaken) in the periods of increased (decreased) solar forcing and temperature. The El Niño–Southern Oscillation (ENSO) variance, based on the standard errors of the ENSO index series from Mann et al. (2009) with a 21-yr window, often decreases when the correlations of the first SVD mode are low. Keeping in mind that the variability of the ENSO index rises (decreases) as the solar forcing rises (decreases) and thus temperature goes up (down) (Mann et al. 2009), we consider that the increase (decrease) in temperature along with the intensified (weakened) solar radiation leads to stronger (decreased) ENSO variability, which is associated with increased (decreased) strength of the southern–northern MA and SWNA–NWNA teleconnection. It should be noted that the increase in greenhouse gases since the industrial era in the 1850s appears to outcompete the solar irradiation

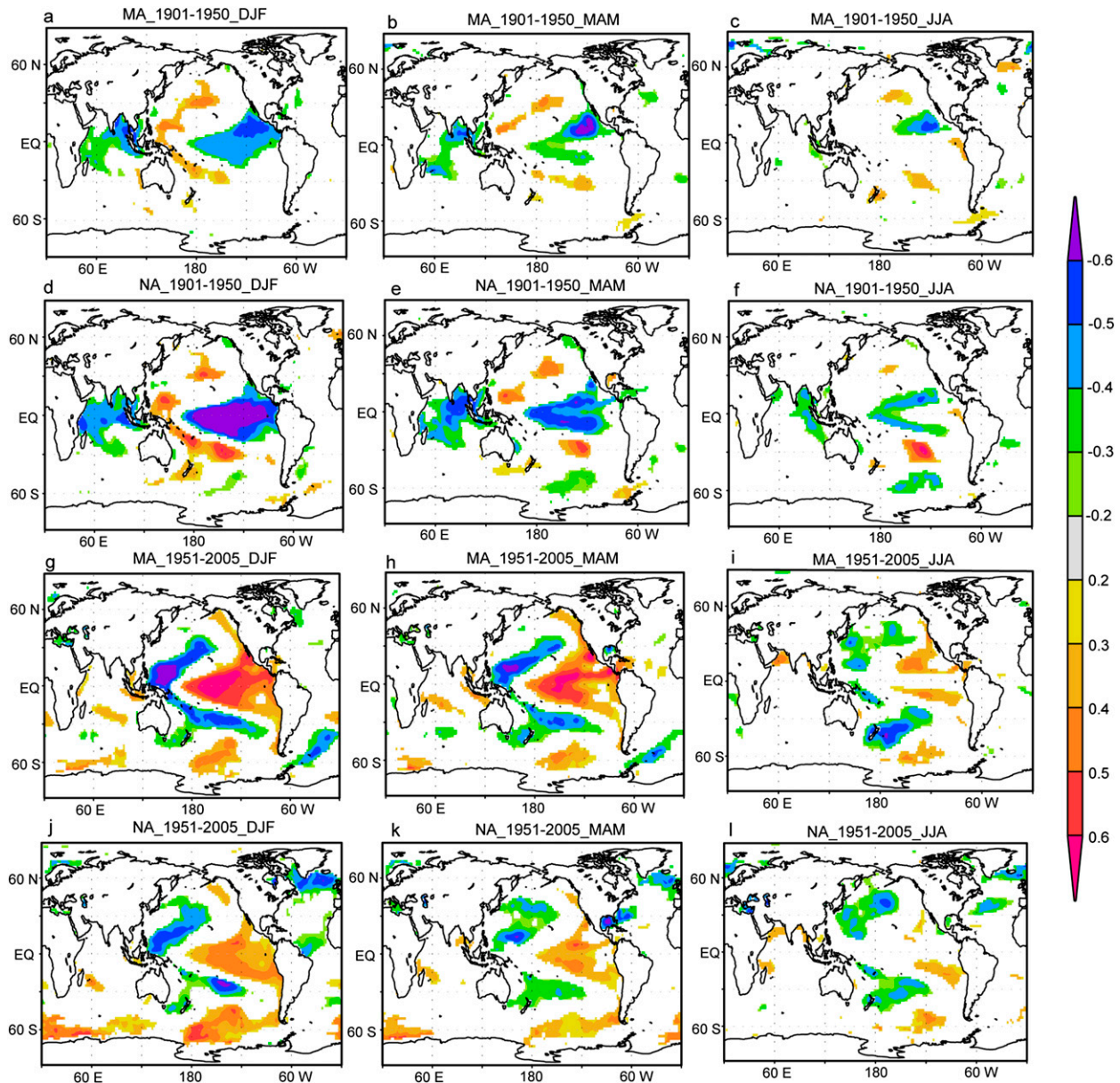


FIG. 9. Significant ( $p < 0.1$ ) correlation maps between SST and the time series of the first leading SVD mode between MADA and NADA during their common period from 1901 to 2005 in winter [December–February (DJF)], spring [March–May (MAM)], and summer [June–August (JJA)]. The SVD modes are based on around a 50-yr time window, as shown in Fig. 7.

in driving the global warming trend since then (Mann et al. 2009). Although the correspondence between solar irradiation and teleconnection is not conspicuous in modern periods, the correspondence between temperature and teleconnection remain robust.

We further investigated the temporal evolution of the first SVD mode at a 50-yr interval. The southern–northern MA and SWNA–NNA teleconnection, particularly the antiphase low MA and SWNA teleconnection, is generally observed for most periods,

except for the periods 1501–1600 (Figs. 7e–h), 1651–1700 (Figs. 7k,l), 1801–50 (Figs. 7q,r), and 1951–2005 (Figs. 2b,d). These periods with weakened (strengthened) teleconnections correspond to the periods with reduced (increased) correlations between time series of the first SVD modes as well as reduced (enhanced) solar forcing, temperature, and ENSO variance. The exception is the weakened southern–northern MA and SWNA–NNA teleconnection at 1951–2005, which does not correspond to low temperature. This may be related to the high

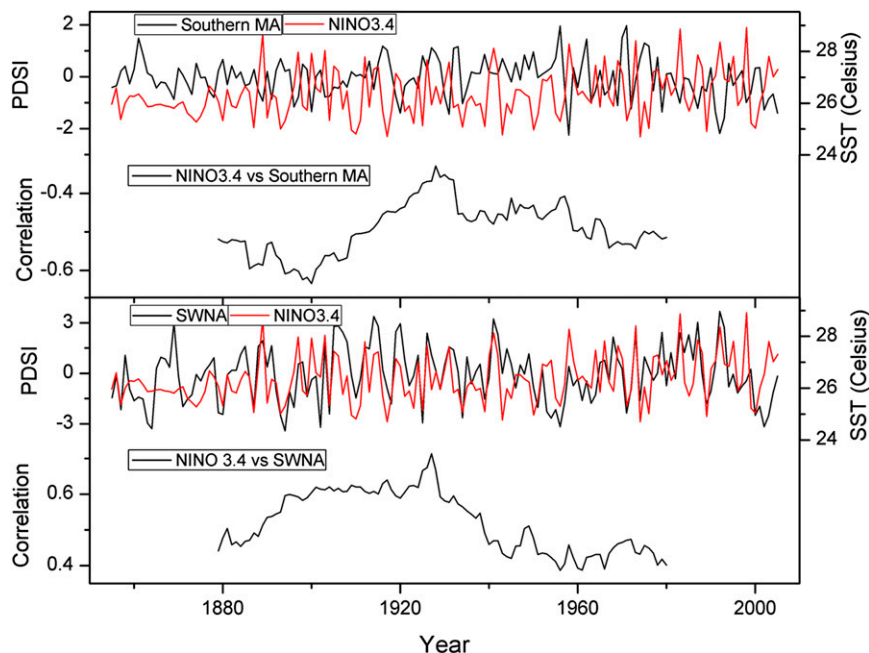


FIG. 10. Visual comparisons and the running correlations based on a 50-yr window (a) between the regional PDSI averaged from southern MA ( $10^{\circ}$ – $30^{\circ}$ N) and the averaged SST for the Niño-3.4 region ( $5^{\circ}$ S– $5^{\circ}$ N,  $120^{\circ}$ – $170^{\circ}$ W) and (b) between SWNA (south of  $40^{\circ}$ N and east of  $95^{\circ}$ W) and the averaged SST for the Niño-3.4 region ( $5^{\circ}$ S– $5^{\circ}$ N,  $120^{\circ}$ – $170^{\circ}$ W).

variability of the PDSI in the middle and high latitudes since the 1950s owing to an increased evaporation and drying trend in these arid and semiarid regions. Thereby, the teleconnection patterns in the middle and high latitudes outcompetes the southern–northern MA and SWNA–NNA teleconnection since the 1950s. As indicated by Fig. 6, the ENSO may have played an important role in modulating the southern–northern MA and SWNA–NNA teleconnection. We further calculated the SVD pattern between high-passed MADA and NADA using a Gaussian filter to highlight the variations at time scales shorter than 8 yr (Fig. 8), a frequency band of ENSO variability. The covarying patterns for the high-passed data generally show an antiphase southern MA and SWNA teleconnection in most subperiods, except for the 1451–1550, 1651–1750, and 1801–50 periods (Fig. 8), which is similar to the temporal variations inferred from the raw MADA and NADA. This again indicates that the southern–northern MA and SWNA–NNA teleconnection is more pronounced on the interannual scale, possibly related to the ENSO variability.

#### 4. Teleconnection and coupled ocean–atmosphere interactions

The spatial correlations between the first SVD time series and the SST during their common period 1901–2005

show an ENSO-like pattern with inverse correlations with SST in the eastern and western tropical Pacific (Fig. 9), supporting our previous findings about the dominance of ENSO on the southern–northern MA and SWNA–NNA teleconnection. The associations with ENSO are most significant in the twentieth century and ENSO is more influential on the hydroclimate teleconnections during its peak phase in wintertime (December–February) (Figs. 9a,d,g,j). In the low-latitude regions, the warm (cold) phase of ENSO with warm (cold) SST and low (high) sea level pressure in the eastern equatorial Pacific correspond to cold (warm) SST and high (low) sea level pressure in the western equatorial Pacific via the weakened (strengthened) Walker circulation, leading to a pluvial (dry) southwestern NA and dry (pluvial) monsoon-dominated region (Buckley et al. 2010; Cook et al. 2007; Fang et al. 2011b; Feng and Hu 2004; Kumar et al. 1999; Lau and Weng 2002; Li et al. 2014; Seager 2007). The relationships are further validated by the negative associations between the averaged SST over the Niño-3.4 region with the averaged PDSI over southern MA and the positive associations between mean SST in the Niño-3.4 region and the SWNA (Fig. 10). In regard to GPHs in the middle troposphere, the tropical trough associated with high SST anomalies in the western Pacific expands to the eastern Pacific (Fig. 11). This GPH belt resembles the intertropical



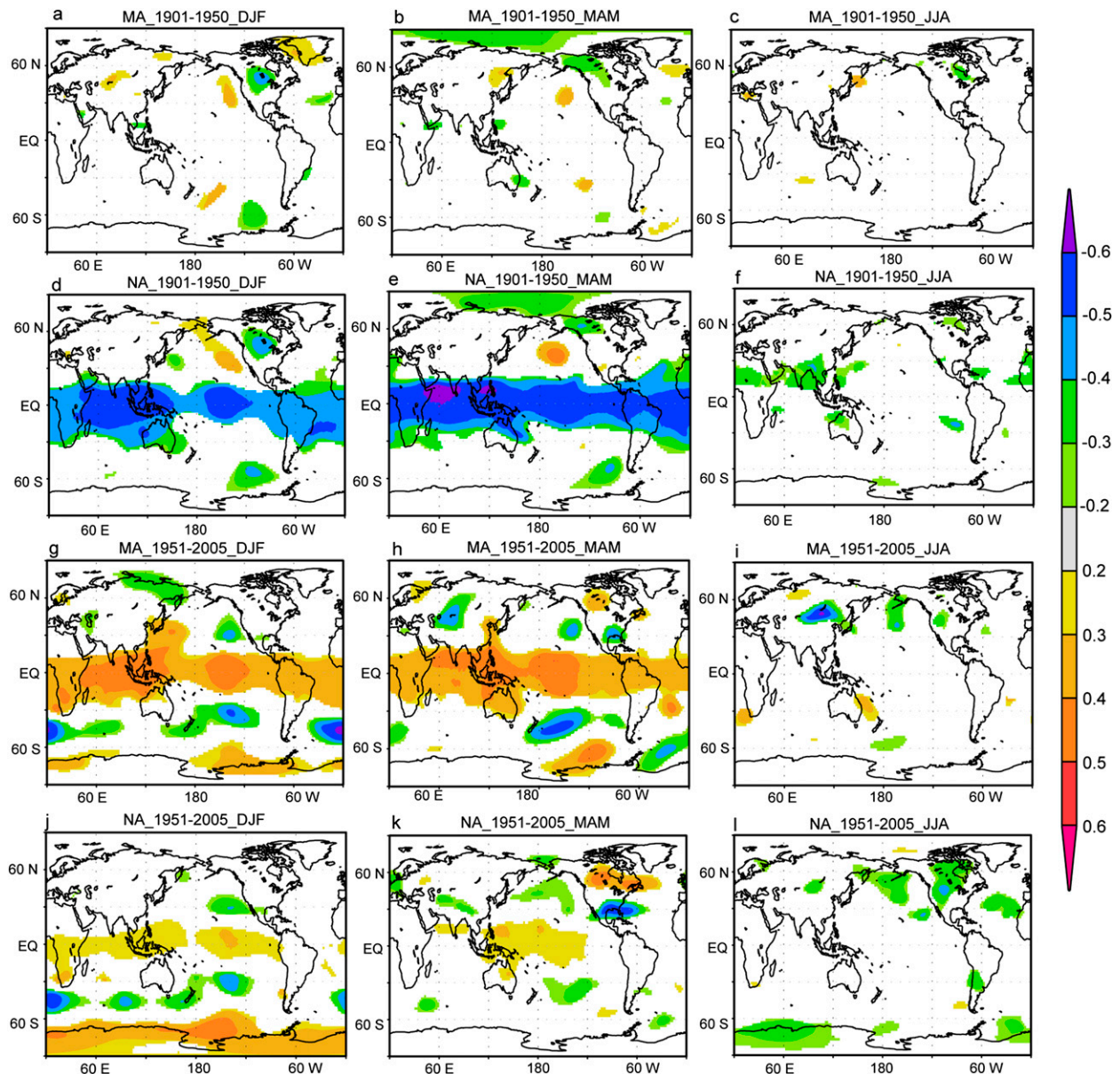


FIG. 11. Maps of significant ( $p < 0.1$ ) correlation between GPHs at 500 hPa and the time series of the first leading SVD mode between MADA and NADA during the subperiods of (a)–(f) 1901–50 and (g)–(l) 1951–2005 in winter (DJF), spring (MAM), and summer (JJA). The SVD modes are based on around a 50-yr time interval, as shown in Fig. 7.

convergence zone (ITCZ) that focuses on the equatorial zone where the northeast and southeast trade winds meet. The warm (cold) phase ENSO often corresponds to a weakened (enhanced) ITCZ and thus to a weakened (enhanced) Asian summer monsoon (Yancheva et al. 2007), which is consistent with our findings (Figs. 9 and 11). The SST anomalies in the tropical ocean and coupled near-equatorial pressure belt associated with the hydroclimate anomalies in MA and NA further indicate that the southern–northern MA and SWNA–NWNNA teleconnection is mainly linked via the low-latitude

ocean–atmosphere interactions. The important role of the Walker circulation and ITCZ in linking the hydroclimate changes in MA and NA are evidenced by the most significant correlations with wind vectors in the tropical Pacific. During the warm (cold) phase of ENSO, the wind anomalies propagate from the tropical (subtropical) to the subtropical (tropical) Pacific Ocean and from the western (eastern) to the eastern (western) Pacific Ocean (Fig. 12).

We also found that the ENSO pattern dominates the hydroclimate teleconnection derived from the high-passed

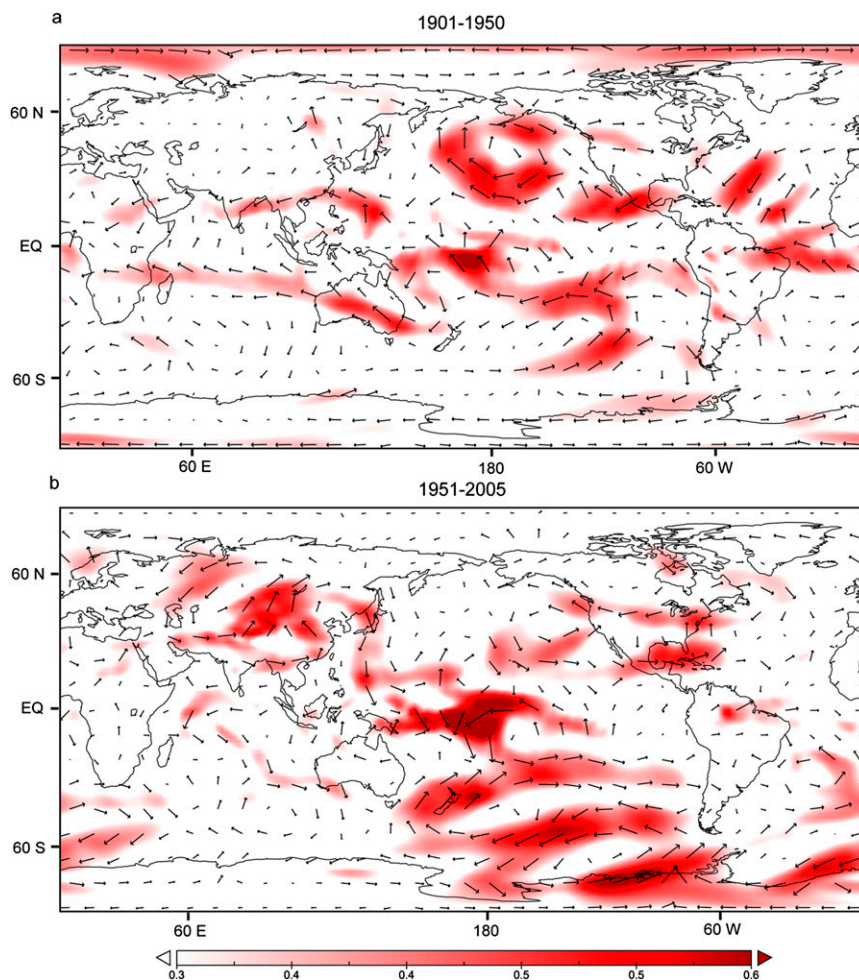


FIG. 12. Maps of correlation between wind vectors at 500 hPa and the time series of the first leading SVD mode between MADA and NADA during the subperiods of (a) 1901–50 and (b) 1951–2005 in spring (MAM). The significant ( $p < 0.01$ ) correlations are highlighted by red.

data ( $>8$  yr) (Figs. 8 and 13), while there are no significant correlations with coupled ocean–atmosphere patterns in the Indian and western Pacific Oceans and middle and extratropical regions as for the raw data. Accordingly, the high-passed data show the low MA and SWNA dipole pattern but show less significant loadings over the middle and high latitudes in the southern–northern MA and SWNA–NWNNA teleconnection. This may suggest that, although ENSO is the major regulator of the antiphase low MA and SWNA teleconnection, the southern–northern MA and SWNA–NWNNA teleconnection cannot be reproduced without the impacts of the ocean–atmosphere interactions in the Indian and western Pacific Oceans. The tropical Indian Ocean SST can act as a “capacitor” in generating delayed hydroclimate responses of the Indo–western Pacific climate to ENSO (Xie et al. 2009). This capacitor effect likely adds an “autocorrelation” to the

Indo–western Pacific climate and helps establish the decadal/multidecadal covarying patterns. Therefore, the high-passed data showed insignificant correlations with ocean–atmosphere interactions in these regions. Since the effects of the ocean–atmosphere interactions in the Indian and western Pacific Oceans and the delayed responses to ENSO are not taken into account for the high-passed data, the high-passed data respond significantly to concurrent ENSO only in summertime (Fig. 14).

During the cold phase of ENSO, the strengthened Asian summer monsoon may be accompanied by intensified subsidence over the central high Asia, possibly contributing to the southern–northern MA dipole (Broccoli and Manabe 1992). During the warm phase of ENSO, we observed no significant wind anomalies from the ocean in the low MA but observed significant southwest wind anomalies in the high MA (Fig. 12),



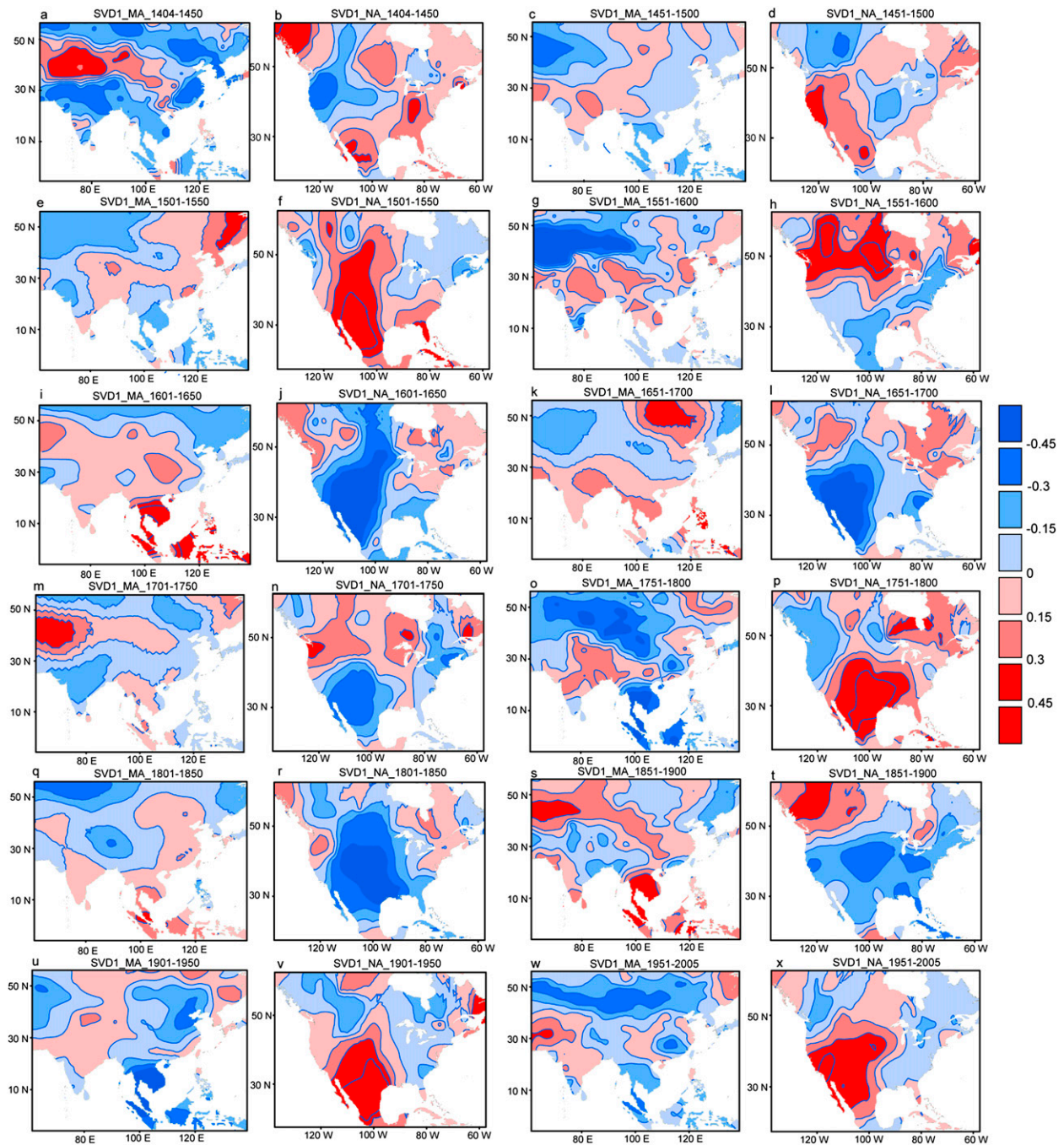


FIG. 13. Heterogeneous correlation maps for the MA and NA derived from the first leading SVD mode between MADA and NADA based on around a 50-yr time window for the high-passed data ( $<8$  yr). The most recent SVD mode for the period 1951–2005 is shown in Fig. 2.

leading to a wet condition. This is consistent with previous results that anomalous high (low) over the western Pacific and Indian Oceans in response to a warm (cold) phase of ENSO can facilitate (inhibit) the transport of moisture from Indian Ocean, particularly from the Arabian Sea, to high MA along its northwestern flank (Mariotti 2007; Yang and Zhang 2007). Accordingly,

a wave train was observed from the Indian Ocean (anticyclone pattern) to Siberia (anticyclone) with a cyclonic pattern over central Asia (Yang and Zhang 2007). Meanwhile, moisture taken by the westerlies is favored when a cyclonelike pattern exists in central Asia in a “silk road” teleconnection (Ding and Wang 2005; Enomoto et al. 2003). Therefore, the wave train from the



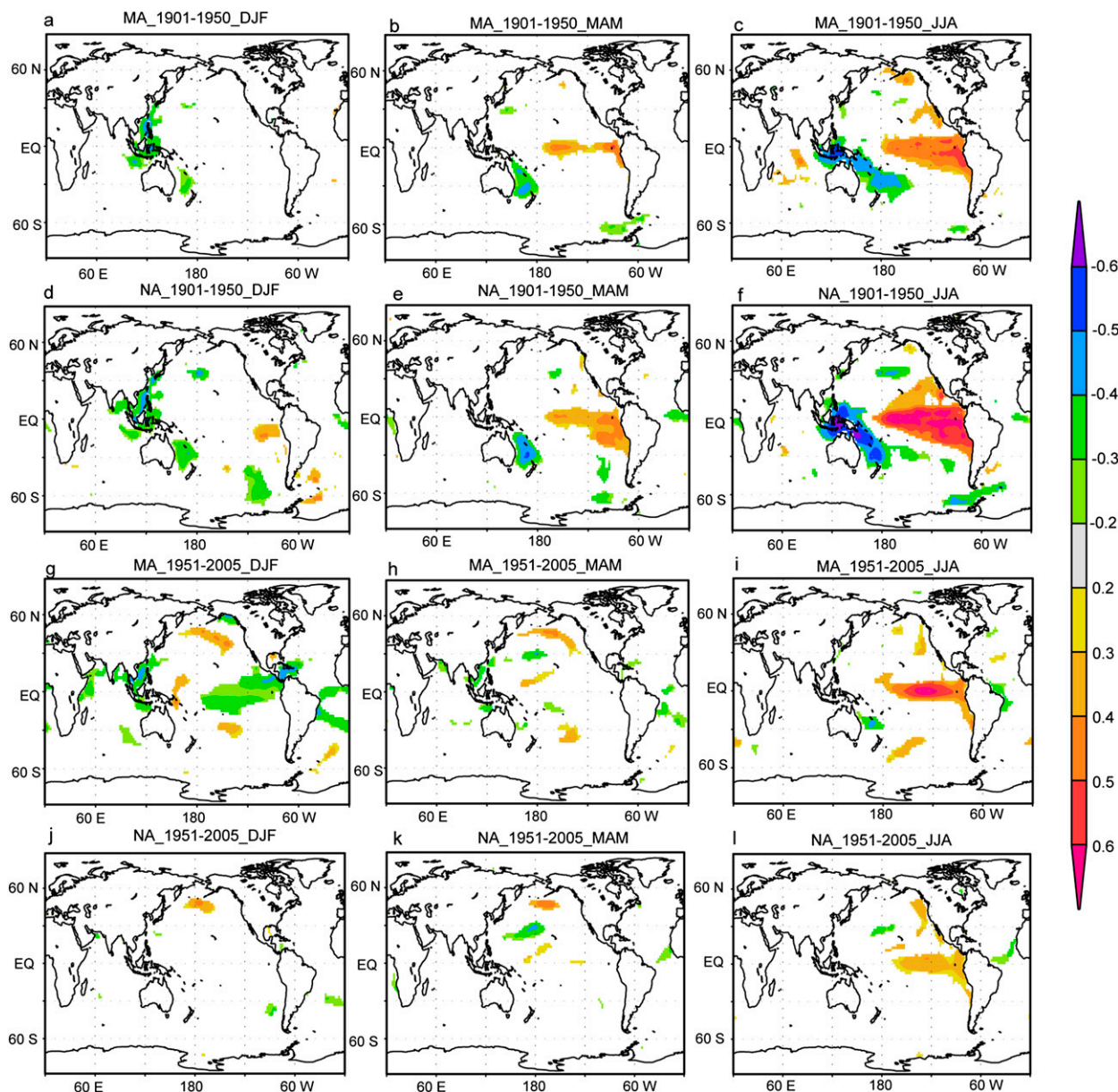


FIG. 14. Significant ( $p < 0.1$ ) correlation maps between SST and the time series of the first leading SVD mode between high-passed ( $< 8$  yr) MADA and NADA during their common period from 1901 to 2005 in winter (DJF), spring (MAM), and summer (JJA). The SVD modes are based on around a 50-yr time window, as shown in Fig. 3.

Arabian Sea may deepen the cyclone pattern over central Asia and thus promote moisture transport by mid-latitude westerlies. This study agrees with the previous regionalization of modern precipitation that indicated a farther north boundary of the region influenced by the Asian summer monsoon (Conroy and Overpeck 2011). However, it is likely that precipitation from other seasons than summer is dominated by westerlies, as indicated by some studies (Broccoli and Manabe 1992; Enomoto et al. 2003).

In NA, an anomalous high (low) and the coupled anomalous warm (cold) SST in the North Pacific Ocean was accompanied with an anticyclone (cyclone) pattern in the north-central Pacific Ocean, which transports more (less) moisture into high NA and less (more) moisture into low NA (Fig. 12). This may contribute to the establishment of the SWNA–NNA dipole and possibly reflects its associations with the Pacific decadal oscillation (PDO) (Mantua and Hare 2002) and the Pacific–North American (PNA) teleconnection

(Leathers et al. 1991). The SST anomalies in the north-central Pacific Ocean may be related to the ENSO variability since some studies suggest that the PDO is the reddening of the ENSO (Mantua and Hare 2002). The GPH anomalies may be part of the wave train dispersed from the Indo-western Pacific Oceans, which links the subtropical hydroclimate changes in East Asia and North America (Lau and Weng 2002). In addition, the pluvial (dry) low-latitude MA and NA with increased (decreased) advection can be accompanied by a strengthened (weakened) descending limb and thus dry (pluvial) phase in the high-latitude MA (Broccoli and Manabe 1992; Fu et al. 1999), contributing to the development of the dipole hydroclimate patterns of southern-northern MA and SWNA-NWNA. Interestingly, a wave train and associated cyclone-anticyclone patterns from the Antarctic region to East Asia were observed through the route of the Asian-Australian monsoon (Figs. 11 and 12). The linkages between the Antarctic Oscillation (AAO) and hydroclimate variations in MA were also identified in previous studies (Wang and Fan 2006). It appears that the ENSO is the major regulator of the southern-northern MA and SWNA-NWNA teleconnection, particularly at the interannual scale, and extratropical ocean-atmosphere patterns play an important role in modulating the extratropical hydroclimate teleconnections.

## 5. Conclusions

We investigated hydroclimate teleconnections and their temporal evolution between MADA and NADA during the past 600 years using the singular value decomposition (SVD) method at interannual and decadal time scales, as well as their associations with global SSTs and GPHs from wintertime to the summertime. The biases in reconstruction are observed at a regional scale and have limited influences on the large-scale teleconnection pattern. The southern-northern MA and SWNA-NWNA hydroclimate teleconnection is composed of the southern-northern MA dipole and the SWNA-NWNA dipole and is most robust during the entire reconstruction period at both interannual and decadal/multidecadal scales. This teleconnection is dominated by the antiphase low MA and SWNA teleconnection in low latitudes, which is more significant at the interannual scale and is mainly regulated by ENSO. The southern-northern MA and SWNA-NWNA teleconnection is associated not only with ENSO but also with the extratropical ocean-atmosphere patterns. This teleconnection is strengthened (weakened) when the ENSO variability is strengthened (weakened)

in periods with increased (decreased) solar forcing and temperature.

**Acknowledgments.** This study is funded by the fellowship of the Nordic top-level research initiative Cryosphere-Atmosphere Interactions in a Changing Arctic Climate (CRAICC), the National Science Foundation of China (41001115 and 41171039), and the Minjiang Special-term Professor fellowship. The very helpful comments from three anonymous reviewers are highly appreciated.

## REFERENCES

- Bard, E., G. Raisbeck, F. Yiou, and J. Jouzel, 2000: Solar irradiance during the last 1200 years based on cosmogenic nuclides. *Tellus*, **52B**, 985–992, doi:10.1034/j.1600-0889.2000.d01-7.x.
- Bretherton, C. S., C. Smith, and J. M. Wallace, 1992: An intercomparison of methods for finding coupled patterns in climate data. *J. Climate*, **5**, 541–560, doi:10.1175/1520-0442(1992)005<0541:AIOMFF>2.0.CO;2.
- Broccoli, A. J., and S. Manabe, 1992: The effects of orography on midlatitude Northern Hemisphere dry climates. *J. Climate*, **5**, 1181–1201, doi:10.1175/1520-0442(1992)005<1181:TEOOM>2.0.CO;2.
- Buckley, B. M., and Coauthors, 2010: Climate as a contributing factor in the demise of Angkor, Cambodia. *Proc. Natl. Acad. Sci. USA*, **107**, 6748–6752, doi:10.1073/pnas.0910827107.
- Compo, G. P., and Coauthors, 2011: The Twentieth Century Reanalysis project. *Quart. J. Roy. Meteor. Soc.*, **137**, 1–28, doi:10.1002/qj.776.
- Conroy, J. L., and J. T. Overpeck, 2011: Regionalization of present-day precipitation in the greater monsoon region of Asia. *J. Climate*, **24**, 4073–4095, doi:10.1175/2011JCLI4033.1.
- Cook, E., D. M. Meko, D. W. Stahle, and M. K. Cleaveland, 1999: Drought reconstructions for the continental United States. *J. Climate*, **12**, 1145–1162, doi:10.1175/1520-0442(1999)012<1145:DRFTCU>2.0.CO;2.
- , C. A. Woodhouse, C. M. Eakin, D. M. Meko, and D. W. Stahle, 2004: Long-term aridity changes in the western United States. *Science*, **306**, 1015, doi:10.1126/science.1102586.
- , R. Seager, M. A. Cane, and D. W. Stahle, 2007: North American drought: Reconstructions, causes, and consequences. *Earth-Sci. Rev.*, **81**, 93–134, doi:10.1016/j.earscirev.2006.12.002.
- , K. J. Anchukaitis, B. M. Buckley, R. D. D'Arrigo, G. C. Jacoby, and W. E. Wright, 2010: Asian monsoon failure and megadrought during the last millennium. *Science*, **328**, 486–489, doi:10.1126/science.1185188.
- Dai, A., K. E. Trenberth, and T. Qian, 2004: A global dataset of Palmer drought severity index for 1870–2002: Relationship with soil moisture and effects of surface warming. *J. Hydrometeorol.*, **5**, 1117–1130, doi:10.1175/JHM-386.1.
- Ding, Q., and B. Wang, 2005: Circumglobal teleconnection in the Northern Hemisphere summer. *J. Climate*, **18**, 3483–3505, doi:10.1175/JCLI3473.1.
- Duan, A. M., and G. X. Wu, 2005: Role of the Tibetan Plateau thermal forcing in the summer climate patterns over subtropical Asia. *Climate Dyn.*, **24**, 793–807, doi:10.1007/s00382-004-0488-8.

- Eddy, J. A., 1976: The Maunder Minimum. *Science*, **192**, 1189–1202, doi:[10.1126/science.192.4245.1189](https://doi.org/10.1126/science.192.4245.1189).
- Enomoto, T., B. J. Hoskins, and Y. Matsuda, 2003: The formation mechanism of the Bonin high in August. *Quart. J. Roy. Meteor. Soc.*, **129**, 157–178, doi:[10.1256/qj.01.211](https://doi.org/10.1256/qj.01.211).
- Fang, K., N. Davi, X. Gou, F. Chen, E. Cook, J. Li, and R. D'Arrigo, 2010: Spatial drought reconstructions for central high Asia based on tree rings. *Climate Dyn.*, **35**, 941–951, doi:[10.1007/s00382-009-0739-9](https://doi.org/10.1007/s00382-009-0739-9).
- , X. Gou, F. Chen, E. Cook, J. Li, B. Buckley, and R. D'Arrigo, 2011a: Large-scale precipitation variability over northwest China inferred from tree rings. *J. Climate*, **24**, 3457–3468, doi:[10.1175/2011JCLI3911.1](https://doi.org/10.1175/2011JCLI3911.1).
- , —, —, J. Li, F. Zhou, and Y. Li, 2011b: Covariability between tree-ring based precipitation reconstructions in northwest China and sea surface temperature of Indian and Pacific oceans. *Climate Res.*, **49**, 17–27, doi:[10.3354/cr01019](https://doi.org/10.3354/cr01019).
- , —, —, N. Davi, and C. Liu, 2012: Spatiotemporal drought variability for central and eastern Asia over the past seven centuries derived from tree-ring based reconstructions. *Quat. Int.*, **283**, 107–116, doi:[10.1016/j.quaint.2012.03.038](https://doi.org/10.1016/j.quaint.2012.03.038).
- Feng, S., and Q. Hu, 2004: Variations in the teleconnection of ENSO and summer rainfall in northern China: A role of the Indian summer monsoon. *J. Climate*, **17**, 4871–4881, doi:[10.1175/JCLI-3245.1](https://doi.org/10.1175/JCLI-3245.1).
- Fu, C., H. F. Diaz, D. Dong, and J. O. Fletcher, 1999: Changes in atmospheric circulation over Northern Hemisphere oceans associated with the rapid warming of the 1920s. *Int. J. Climatol.*, **19**, 581–606, doi:[10.1002/\(SICI\)1097-0088\(199905\)19:6<581::AID-JOC396>3.0.CO;2-P](https://doi.org/10.1002/(SICI)1097-0088(199905)19:6<581::AID-JOC396>3.0.CO;2-P).
- Herweijer, C., and R. Seager, 2008: The global footprint of persistent extra-tropical drought in the instrumental era. *Int. J. Climatol.*, **28**, 1761–1774, doi:[10.1002/joc.1590](https://doi.org/10.1002/joc.1590).
- Hoerling, M., and A. Kumar, 2003: The perfect ocean for drought. *Science*, **299**, 691–694, doi:[10.1126/science.1079053](https://doi.org/10.1126/science.1079053).
- Kalnay, E., and Coauthors, 1996: The NCEP/NCAR 40-Year Reanalysis Project. *Bull. Amer. Meteor. Soc.*, **77**, 437–471, doi:[10.1175/1520-0477\(1996\)077<0437:TNYRP>2.0.CO;2](https://doi.org/10.1175/1520-0477(1996)077<0437:TNYRP>2.0.CO;2).
- Kistler, R., and Coauthors, 2001: The NCEP-NCAR 50-Year Reanalysis: Monthly means CD-ROM and documentation. *Bull. Amer. Meteor. Soc.*, **82**, 247–268, doi:[10.1175/1520-0477\(2001\)082<0247:TNNYRM>2.3.CO;2](https://doi.org/10.1175/1520-0477(2001)082<0247:TNNYRM>2.3.CO;2).
- Kumar, K. K., B. Rajagopalan, and M. A. Cane, 1999: On the weakening relationship between the Indian monsoon and ENSO. *Science*, **284**, 2156–2159, doi:[10.1126/science.284.5423.2156](https://doi.org/10.1126/science.284.5423.2156).
- Lau, K. M., and H. Weng, 2002: Recurrent teleconnection patterns linking summertime precipitation variability over East Asia and North America. *J. Meteor. Soc. Japan*, **80**, 1309–1324, doi:[10.2151/jmsj.80.1309](https://doi.org/10.2151/jmsj.80.1309).
- Leathers, D. J., B. Yarnal, and M. A. Palecki, 1991: The Pacific/North American teleconnection pattern and United States climate. Part I: Regional temperature and precipitation associations. *J. Climate*, **4**, 517–528, doi:[10.1175/1520-0442\(1991\)004<0517:TPATPA>2.0.CO;2](https://doi.org/10.1175/1520-0442(1991)004<0517:TPATPA>2.0.CO;2).
- Li, J., and Coauthors, 2009: Summer monsoon moisture variability over China and Mongolia during the past four centuries. *Geophys. Res. Lett.*, **36**, L22705, doi:[10.1029/2009GL041162](https://doi.org/10.1029/2009GL041162).
- , S.-P. Xie, E. R. Cook, G. Huang, R. D'Arrigo, F. Liu, J. Ma, and X.-T. Zheng, 2011: Interdecadal modulation of El Niño amplitude during the past millennium. *Nat. Climate Change*, **1**, 114–118, doi:[10.1038/nclimate1086](https://doi.org/10.1038/nclimate1086).
- , —, and —, 2014: El Niño phases and modes embedded in Asian and North American drought reconstructions. *Quat. Sci. Rev.*, **85**, 20–34, doi:[10.1016/j.quascirev.2013.11.014](https://doi.org/10.1016/j.quascirev.2013.11.014).
- Lu, R., 2005: Interannual variation of North China rainfall in rainy season and SSTs in the equatorial eastern Pacific. *Chin. Sci. Bull.*, **50**, 2069–2073, doi:[10.1007/BF03322803](https://doi.org/10.1007/BF03322803).
- Mann, M. E., and Coauthors, 2009: Global signatures and dynamical origins of the Little Ice Age and Medieval Climate Anomaly. *Science*, **326**, 1256–1260, doi:[10.1126/science.1177303](https://doi.org/10.1126/science.1177303).
- Mantua, N. J., and S. R. Hare, 2002: The Pacific decadal oscillation. *J. Oceanogr.*, **58**, 35–44, doi:[10.1023/A:1015820616384](https://doi.org/10.1023/A:1015820616384).
- Mariotti, A., 2007: How ENSO impacts precipitation in southwest central Asia. *Geophys. Res. Lett.*, **34**, L16706, doi:[10.1029/2007GL030078](https://doi.org/10.1029/2007GL030078).
- Seager, R., 2007: The turn of the century North American drought: Global context, dynamics, and past analogs. *J. Climate*, **20**, 5527–5552, doi:[10.1175/2007JCLI1529.1](https://doi.org/10.1175/2007JCLI1529.1).
- Shindell, D. T., G. A. Schmidt, M. E. Mann, D. Rind, and A. Waple, 2001: Solar forcing of regional climate change during the Maunder Minimum. *Science*, **294**, 2149–2152, doi:[10.1126/science.1064363](https://doi.org/10.1126/science.1064363).
- Smith, T. M., R. W. Reynolds, T. C. Peterson, and J. Lawrimore, 2008: Improvements to NOAA's historical merged land-ocean surface temperature analysis (1880–2006). *J. Climate*, **21**, 2283–2296, doi:[10.1175/2007JCLI2100.1](https://doi.org/10.1175/2007JCLI2100.1).
- St. George, S., D. Meko, and E. Cook, 2010: The seasonality of precipitation signals embedded within the North American Drought Atlas. *Holocene*, **20**, 983–988, doi:[10.1177/0959683610365937](https://doi.org/10.1177/0959683610365937).
- Sturaro, G., 2003: A closer look at the climatological discontinuities present in the NCEP/NCAR reanalysis temperature due to the introduction of satellite data. *Climate Dyn.*, **21**, 309–316, doi:[10.1007/s00382-003-0334-4](https://doi.org/10.1007/s00382-003-0334-4).
- Trenberth, K. E., G. W. Branstator, D. Karoly, A. Kumar, N.-C. Lau, and C. Ropelewski, 1998: Progress during TOGA in understanding and modeling global teleconnections associated with tropical. *J. Geophys. Res.*, **103**, 14 291–14 324, doi:[10.1029/97JC01444](https://doi.org/10.1029/97JC01444).
- Ummenhofer, C. C., R. D. D'Arrigo, K. J. Anchukaitis, B. M. Buckley, and E. R. Cook, 2012: Links between Indo-Pacific climate variability and drought in the Monsoon Asia Drought Atlas. *Climate Dyn.*, **40**, 1319–1334, doi:[10.1007/s00382-012-1458-1](https://doi.org/10.1007/s00382-012-1458-1).
- Wang, H., and K. Fan, 2006: Southern Hemisphere mean zonal wind in upper troposphere and East Asian summer monsoon circulation. *Chin. Sci. Bull.*, **51**, 1508–1514, doi:[10.1007/s11434-006-2009-0](https://doi.org/10.1007/s11434-006-2009-0).
- Wells, N., S. Goddard, and M. J. Hayes, 2004: A self-calibrating Palmer drought severity index. *J. Climate*, **17**, 2335–2351, doi:[10.1175/1520-0442\(2004\)017<2335:ASPSI>2.0.CO;2](https://doi.org/10.1175/1520-0442(2004)017<2335:ASPSI>2.0.CO;2).
- Xie, S. P., K. Hu, J. Hafner, H. Tokinaga, Y. Du, G. Huang, and T. Sampe, 2009: Indian Ocean capacitor effect on Indo-western Pacific climate during the summer following El Niño. *J. Climate*, **22**, 730–747, doi:[10.1175/2008JCLI2544.1](https://doi.org/10.1175/2008JCLI2544.1).
- Yancheva, G., and Coauthors, 2007: Influence of the intertropical convergence zone on the East Asian monsoon. *Nature*, **445**, 74–77, doi:[10.1038/nature05431](https://doi.org/10.1038/nature05431).
- Yang, F., and K. M. Lau, 2004: Trend and variability of China precipitation in spring and summer: Linkage to sea surface temperatures. *Int. J. Climatol.*, **24**, 1625–1644, doi:[10.1002/joc.1094](https://doi.org/10.1002/joc.1094).
- Yang, L. M., and Q. Y. Zhang, 2007: Circulation characteristics of interannual and interdecadal anomalies of summer rainfall in north Xinjiang (in Chinese). *Chin. J. Geophys.*, **50**, 412–419.